

Verification of High-Resolution Satellite-Based Rainfall Estimates around Japan Using a Gauge-Calibrated Ground-Radar Dataset

Takuji KUBOTA

Earth Observation Research Center, Japan Aerospace and Exploration Agency, Tsukuba, Japan

Tomoo USHIO

Department of Electrical, Electronic, and Information Engineering, Osaka University, Suita, Japan

Shoichi SHIGE, Satoshi KIDA

Department of Aerospace Engineering, Osaka Prefecture University, Sakai, Japan

Misako KACHI

Earth Observation Research Center, Japan Aerospace and Exploration Agency, Tsukuba, Japan

and

Ken'ichi OKAMOTO

Faculty of Environmental and Information Studies, Tottori University of Environmental Studies, Tottori, Japan

(Manuscript received 30 June 2008, in final form 31 October 2008)

Abstract

Global rainfall products of high spatial and temporal resolutions have been provided using combined data from passive microwave (PMW) sensors in low Earth orbit and infrared (IR) radiometers in geostationary Earth orbit (GEO). This study compared six satellite rainfall estimates around Japan with reference to a ground-radar dataset calibrated by rain gauges provided by the Japan Meteorological Agency (JMA) from January through December 2004. Validation results tended to be better for the products with temporal interpolation based upon the morphed technique using GEO IR information. Satellite estimates were poor for light rainfall during the warm season and for very heavy rainfall.

Further analyses of satellite estimates were conducted in terms of data sources and surface types. Effective performance by the merger of PMW sounders over the ocean was verified by radar validation, in addition to the best results of the PMW imagers. Overall, validation results over the ocean were best, and results over mountainous regions were worst. Performance was poor over coasts and small islands, due to the problem of PMW retrievals. This study focused on hydrometeor profiles of orographic heavy rainfall over the Japanese Archipelago, which could be related to the poor performance of satellite estimates in very heavy rainfall.

Corresponding author: Takuji Kubota, Earth Observation Research Center, Japan Aerospace Exploration Agency, 2-1-1 Sengen, Tsukuba-city, Ibaraki 305-8505, Japan
E-mail: kubota@ieee.org
©2009, Meteorological Society of Japan

1. Introduction

There has recently been increasing interest in high-resolution precipitation datasets based on satellite remote sensing. Global precipitation products capable of high spatial (0.25° or finer) and temporal (three-hour

or shorter) resolutions have been provided by developers using combined data from passive microwave (PMW) sensors in low Earth orbit (LEO) and infrared (IR) radiometers in geostationary Earth orbit (GEO) (e.g., Sorooshian et al. 2000; Joyce et al. 2004; Turk and Miller 2005; Huffman et al. 2007; Ushio et al. 2009). For practical use of these datasets, Gottschalck et al. (2005) considered them as potential input to the Global Land Data Assimilation System, and Hong et al. (2007) proposed flood and landslide applications of near-real-time satellite rainfall data.

The development of precipitation datasets has been enhanced since the launch of the Tropical Rainfall Measuring Mission (TRMM) satellite in 1997. Developed under a United States-Japan joint mission, TRMM carries rain observation sensors such as the TRMM Microwave Imager (TMI) and the Precipitation Radar (PR) (Kummerow et al. 1998). Accurate measurement of precipitation by the PR and simultaneous observations by the TMI and PR have greatly advanced algorithm development. An expanded follow-on mission of the TRMM, the Global Precipitation Measurement (GPM) satellite, is planned. This mission will include a TRMM-like core satellite carrying a Dual-Frequency Precipitation Radar (DPR) and a GPM Microwave Imager (GMI), and constellations of satellites equipped with PMW radiometers (Smith et al. 2007).

Satellite precipitation datasets have been evaluated using rain gauges and ground-based radar in regional-scale domains (e.g., Gottschalck et al. 2005; Xie et al. 2007; Tian and Peters-Lidard 2007; Tian et al. 2007). The International Precipitation Working Group (IPWG) and the Program to Evaluate High-Resolution Precipitation Products (PEHRPP) have established a program for in situ validation of daily rainfall estimates by operational satellite algorithms (Arkin et al. 2005; Ebert et al. 2007). The IPWG study built upon satellite precipitation validation studies, such as the Precipitation Intercomparison Project (PIP) (e.g., Smith et al. 1998; Adler et al. 2001) and the Algorithm Intercomparison Projects of the Global Precipitation Climatology Project (GPCP) (e.g., Ebert et al. 1996). As Ebert et al. (2007) pointed out, it is important that strengths and limitations of satellite precipitation data be understood so that the data can be interpreted correctly. The Global Satellite Mapping of Precipitation (GSMaP) Project (Okamoto et al. 2005, 2007) has contributed to IPWG and PEHRPP activities by verifying satellite data around Japan using gauge-calibrated radar data provided by the Japan Meteorological

Agency (JMA).

In this study, satellite rainfall estimates were validated, and their strengths and limitations were examined around Japan. Specifically, GSMaP rainfall estimates by the PMW-IR blended algorithm were validated in detail. Ushio et al. (2009) developed a Kalman filter technique for the GSMaP algorithm, although their paper did not feature evaluations of the products from overall algorithms developed by the GSMaP Project. The present study investigated the GSMaP products; and issues of surface types, sensors, and techniques of algorithms were analyzed for the domain around Japan. Section 2 describes the data and method. Section 3 documents comparisons between various satellite estimates. Section 4 demonstrates the validation of the GSMaP products, in terms of data sources, techniques, and surface types. Section 5 focuses on orographic heavy rainfall. Section 6 presents a summary.

2. Data and method

2.1 Analyzed period

Satellite rainfall estimates were validated with radar data for the period from January through December 2004. Ten record-breaking tropical storms and typhoons made landfall in Japan between June and October (Kim et al. 2005; Nakazawa 2006). Moreover, in mid-July 2004 two well-known heavy rainfall events were observed in Niigata-Fukushima Prefectures and Fukui Prefecture, causing severe economic and social losses in Japan. During 2004, no events of El Niño/Southern Oscillation occurred. The analyzed period was limited to one year, with no guarantee that the present results would be reproduced in other years. However, during 2004, satellite sensors associated with this paper were not changed. Moreover, spatial and temporal resolutions of the radar dataset remained fixed, while the resolutions were upgraded by JMA. Thus, one merit in the analyses of the year 2004 was a constant number of instruments, by which discussions of algorithm problems could be concentrated on.

2.2 Data in this study

The PMW sensors in LEO were generally of two types: imagers and sounders. Through 2004, five PMW imagers were in operation in LEO: the TRMM TMI, the Advanced Microwave Scanning Radiometer for the Earth Observation System (AMSR-E) aboard the National Aeronautics and Space Administration (NASA) satellite Aqua (Kawanishi et al. 2003), and

three Special Sensor Microwave/Imager (SSM/I) units of the Defense Meteorological Satellite Program. The over-ocean algorithm for the PMW imagers in rain retrievals used information of emitted radiation from rainwater with low-frequency channels (e.g., 10 GHz and 19 GHz channels), in addition to scattering with high-frequency channels (e.g., 85 GHz channel); the over-land and over-coast algorithms used only scattering signals because of high and variable emissivity of the land surface (Wilheit et al. 1991; Grody 1991; Petty 1994; Kummerow et al. 2001; McCollum and Ferraro 2003; Olson et al. 2006; Kubota et al. 2007). For scattering techniques, the relationship to the rain rate was less direct than for emission, because the scattering was primarily due to the frozen hydrometeors above freezing level (Wilheit 1986). Three sounders (e.g., the advanced microwave sounding unit-B (AMSU-B) aboard National Oceanic and Atmospheric Administration (NOAA) satellites) were in operation through 2004. Rainfall estimates from the AMSU-B were based on scattering information from high-frequency channels such as the 89 and 150 GHz channels. In GEO, the Geostationary Operational Environment Satellite (GOES-9) Visible Infrared Spin-Scan Radiometer (VISSR) operated over Japan

in 2004.

a. Production by the GSMaP Project

In the GSMaP Project, surface rainfall was estimated by data from PMW and GEO IR radiometers. The name convention of the GSMaP products is summarized in Table 1. The end product of the GSMaP project was called GSMaP_MVK (hereafter, GSMaP). The GSMaP resolution was hourly, at $0.1^\circ \times 0.1^\circ$ latitude/longitude. GSMaP estimates were achieved by the temporal interpolation of PMW retrievals using a PMW-IR blended algorithm composed of a morphed technique (Joyce et al. 2004) and a Kalman filter (Ushio et al. 2009) using IR information. For computation of the PMW retrievals, estimates from the PMW imagers were retrieved by the algorithm of the GSMaP Project (Aonashi and Liu 2000; Kubota et al. 2007, 2009; Aonashi et al. 2009). Rainfall estimates from the AMSU-B were provided by the NOAA Microwave Surface and Precipitation Products System (Zhao and Weng 2002; Ferraro et al. 2005), which was improved by Vila et al. (2007). In overlapped areas of imagers and sounders, averages of both were used over land and coasts, and only imagers were used over the ocean, due to the advantage of low-frequency

Table 1. Naming convention of rainfall products in the GSMaP Project.

Product	Data source	IR technique	Note
GSMaP_MVK (GSMaP)	PMW imagers, PMW sounders, GEO IR radiometers	Morphing and Kalman filter, by forward and backward processes	End product by the GSMaP project
<i>Experimental product name</i>	Data source	IR technique	Note
G_3B41	PMW imagers, PMW sounders, GEO IR radiometers	Same as in TMPA 3B41	Test of the IR technique
G_NRT	PMW imagers, PMW sounders, GEO IR radiometers	Morphing and Kalman filter, by forward process	Test of the IR technique
G_IVK	PMW imagers, GEO IR radiometers	Morphing and Kalman filter, by forward and backward processes	No use of PMW sounders
G_MWI	PMW imagers	None	No use of PMW sounders and GEO IR radiometers

channels of the imagers. The GSMaP project did not normalize the various rainfall estimates.

In addition, experiment datasets were analyzed in this study (Table 1). The product that merges rainfall estimates derived from the PMW-imagers is referred to as G_MWI. The product from the blended algorithm using G_MWI estimates is named as G_IVK. The purpose was to evaluate effects using the PMW sounders. To test the IR technique, the temporal interpolation of PMW retrievals was performed experimentally using estimates of the TRMM Multi-satellite Precipitation Analysis (TMPA) 3B41 data; this product is named as G_3B41.

In the PMW-IR blended algorithm, rainfall estimates were interpolated by propagating forward and backward in time. For faster processing than for GSMaP_MVK, we computed estimates in a process named as G_NRT for near-real-time requirements, using an algorithm of the forward-only process.

b. TRMM Multi-satellite Precipitation Analysis (TMPA) 3B41, 3B42RT, and 3B42

The TMPA 3B42RT product is a combination of the PMW product (3B40) and PMW-calibrated GEO IR product (3B41), provided by the NASA Goddard Space Flight Center. The 3B40 product is calibrated by the TMI Goddard Profiling Algorithm (GPROF; Kummerow et al. 2001; Olson et al. 2006) precipitation estimate for 3B42RT, and the TMI-PR combined algorithm (Haddad et al. 1997) precipitation estimate for the 3B42. The 3B41 product uses 3B40 to correct combined GEO IR data by the histogram-matching technique. Histograms of time-space matched combined PMW precipitation rates and IR brightness temperatures (Tbs) are used to create spatially varying calibration coefficients that convert IR Tbs to precipitation rates. The 3B42RT data are monthly combined with Climate Assessment and Monitoring System (CAMS) monthly rain gauge analysis developed by the Climate Prediction Center (CPC) (Xie and Arkin 1996). This monthly combined analysis is then used to create monthly scaling factors for each grid box, which are applied to 3B42RT to obtain 3B42. 3B42 was the only product using gauge data in addition to satellite data that was analyzed in this study. A full description of the algorithm was given by Huffman et al. (2007). The horizontal resolution was $0.25^\circ \times 0.25^\circ$ latitude/longitude, and the temporal resolutions were 3 hours for 3B42RT and 3B42 and 1 hour for 3B41. Since 3B42 corresponded to the middle of the 3-hourly period, the data were 1.5 hours out of phase with

the other datasets, and radar datasets for validating the TMPA were averaged during the corresponding time period.

c. NOAA Climate Prediction Center Morphing technique (CMORPH)

CMORPH uses motion vectors derived from half-hourly GEO IR imagery to propagate the precipitation estimates derived from PMW data. The shape and intensity of the precipitation features are modified (morphed) during the time between PMW sensor scans by time-weighted linear interpolation. For a full description of the algorithm, see Joyce et al. (2004). The dataset is provided by the NOAA CPC. The resolution is half-hourly at $8 \text{ km} \times 8 \text{ km}$ nominal resolution. The CPC also provides QMORPH estimates, which are similar to CMORPH estimates, except that the PMW precipitation features are propagated via IR data only forward in time, although QMORPH was not analyzed for this study.

d. Precipitation Estimation from Remotely Sensed Information using Artificial Neural Networks (PERSIANN)

The PERSIANN dataset, provided by the University of California, Irvine, uses a neural network technique to estimate rainfall rates from GEO IR data. The neural network is calibrated with PMW data and can be constantly updated as new data become available. The neural network is then used to obtain precipitation estimates. A full description of the algorithm was given by Sorooshian et al. (2000) and Hsu et al. (1997). The resolution of the global data of the PERSIANN is 3-hourly at $0.25^\circ \times 0.25^\circ$ latitude/longitude spatial resolution.

e. Naval Research Laboratory-Blended satellite technique (NRL-Blended)

In the NRL-Blended technique, GEO IR data are first spatially averaged to the resolution of PMW data. The GEO IR data are then paired with the PMW data and used to calculate the IR rainfall threshold and rain-rate distribution for 2° grid boxes. The GEO IR data are then registered onto a global 0.1° grid, and an inverse-distance weighted mean is calculated from the nearest 2° grid box and the surrounding eight 2° grid boxes. A full description of the algorithm was given by Turk and Miller (2005) and Turk and Mehta (2007). The dataset is provided by the Naval Research Laboratory. The resolution is 3-hourly at $0.25^\circ \times 0.25^\circ$ latitude/longitude. Archived NRL-blended data

started on January 28, 2004; the analyzed period was February 1 to December 31, 2004, due to data availability.

f. Radar-Automated Meteorological Data Acquisition System (AMeDAS) precipitation analysis

Radar-AMeDAS precipitation analysis data (hereafter, radar data) are a 1-hour accumulation precipitation estimate produced by JMA (Makihara et al. 1996; Makihara 2000, 2007). The data are created from a composite of JMA operational 10 min cycle radar data, calibrated by rain gauges (AMeDAS network and gauges operated by the Ministry of Land,

Infrastructure and Transport and the prefectural offices). The calibration technique is described in Makihara (2000). JMA has operated 20 ground-based weather radars since October 1999, and their detection range now covers almost all of the Japanese Archipelago. AMeDAS includes 1320 automatic surface weather stations. The density of the AMeDAS rain gauge network is one station in each 17 km by 17 km area.

From June 2003 to December 2005, the spatial resolution was 0.025° latitude and 0.03125° longitude (2.5 km 2.5 km) and the temporal resolution was 30 min. Observation areas were 500 km² per radar. The radar estimate was calibrated by rain gauges in view of the Z-R relationship modification. Over sea, the radar estimates were calibrated by the mean relationship over land in a radar scan, or previous relationship (Shinpo 2001), and the difficulty of modification by rain gauges was recognized. Note that the calibration over the ocean is uncertain and that results may be unreliable there. In this study, the observation areas were limited to within 150 km of the oceanic stations at Nase, Okinawa, and Ishigakijima, and to within 200 km of the other radar sites. Nase, Okinawa, and Ishigakijima are small islands located south of 30°N, and their observation areas are mostly ocean. Figure 1a depicts the analyzed area, which was the same as that analyzed by Kubota et al. (2007) for validation of the TMI retrievals. These limitations were due to

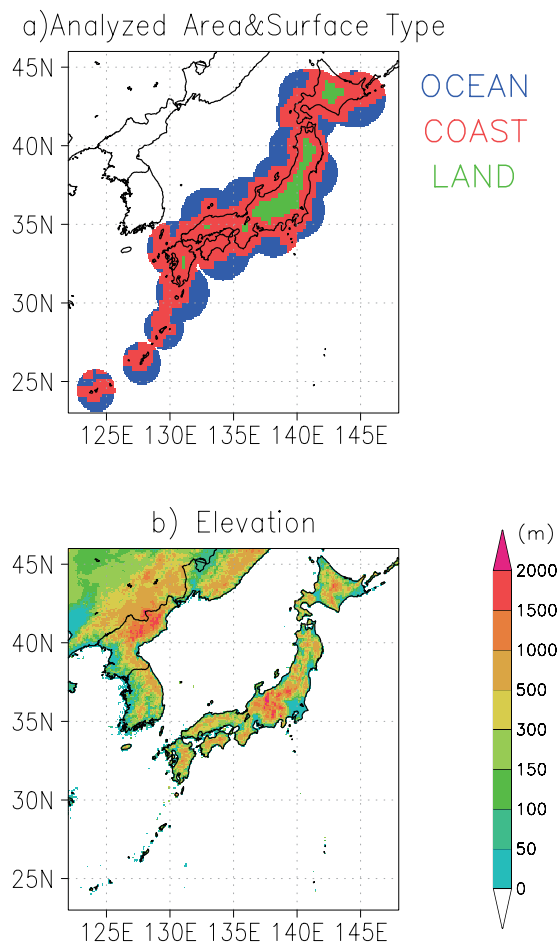


Fig. 1. (a) Analyzed area with surface types from the TSDIS toolkit. Blue denotes ocean, red denotes coast, and green denotes land. (b) GTOPO30 elevation map.

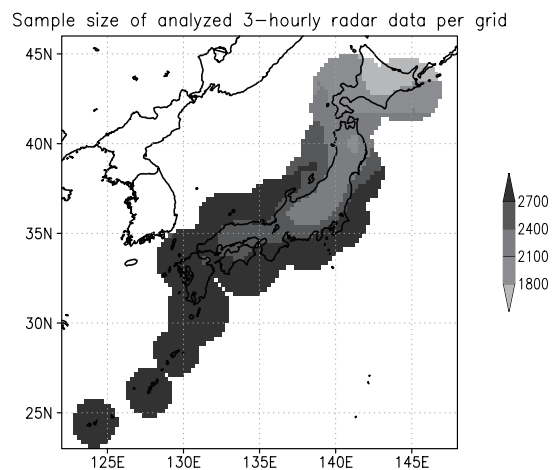


Fig. 2. A distribution of sample size for analyzed 3-hourly radar data per grid with a horizontal resolution of 0.25° × 0.25° latitude/longitude.

apparent biases of the radar data, possibly because of detection losses of low precipitation top heights far from the radar sites and poor calibration over oceanic areas, due to the sparsity of gauges.

2.3 Method of verification using radar data

Satellite estimates were validated for non-snowfall regions because snowfalls were beyond the scope of this study. Using routine surface meteorological data at three weather stations in Japan, Matsuo et al. (1981) found that precipitation types were dependent on surface air temperature and surface relative humidity. Here, a simple threshold of surface temperatures above 4°C was adopted for non-snowfall areas. Surface temperature data were derived by linear interpolation of JMA Global Analysis (GANAL) data. The original resolution of the GANAL data was 6-hourly for 1.25° × 1.25° latitude/longitude. Figure 2 depicts a distribution of sample size for analyzed 3-hourly radar data. The amount of the data decreased in the northern area to about 60%. Note that this threshold may allow warm regions above 4°C with snow-covered land or sea ice.

This study used the four scenarios presented in Table 2, which is a 2 × 2 contingency table, in addition to a well-known correlation coefficient and root mean square error (RMSE). In Table 2, *a* represents correctly estimated rain events, *b* represents events when rain was estimated but did not occur in the validation data, *c* represents events when rain was not estimated but did occur in the validation data, and *d* represents correctly estimated no-rain events. The probability of detection (POD) is the ratio of correct raining estimates to the number of raining events observed. POD was defined as $POD = a / (a + c)$, where elements *a* through *c* are the number of occurrences of each scenario in Table 2. This statistic, also known as the hit rate, is an index of rain detection ability. The false-alarm ratio (FAR) is the fraction of raining esti-

mates that turned out to be wrong, or an index of false rainfall. The FAR was defined as $FAR = b / (a + b)$. Threat score (TS), which is not used in this study, is defined as $TS = a / (a + b + c)$ and gives the number of correct raining estimates divided by the total number of occasions for which a raining event is observed or estimated. A modified version, the equitable threat score (ETS) is defined as

$$ETS = \frac{a - a_{ref}}{a - a_{ref} + b + c},$$

where $a_{ref} = (a + b)(a + c) / n$ and *n* is the sample size. ETS is a modification of the TS that takes into account the number of hits a_{ref} that could be expected, due purely to random chance (cf., Ebert et al. 2007). Because the sample size *n* is required to compute a_{ref} , ETS depends on the number of correct no-raining estimates (the *d* scenario in Table 2), unlike the TS. The frequency bias (FB) is the ratio of the estimated to observed rain areas, $FB = (a + b) / (a + c)$. Here, $FB = 1$ for unbiased estimates, indicating that the number of estimated raining events is the same as the number of

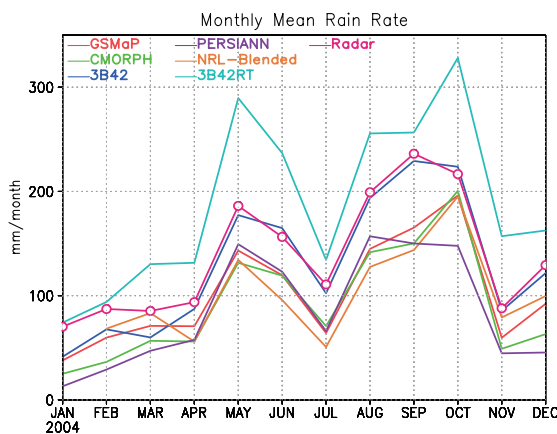


Fig. 3. Monthly time series of satellite-based rainfall estimates and the radar data averaged in the analyzed area for January through December 2004. Red line denotes GSMaP data, green line denotes CMORPH data, blue line denotes 3B42 data, light blue line denotes 3B42RT data, orange line denotes NRL-blended data, and violet line denotes PERSIANN data. The magenta line with open circles denotes radar data. The horizontal resolution of the datasets is 0.25° × 0.25° latitude/longitude.

Table 2. A 2 × 2 contingency table for evaluation. Elements *a* through *d* are assigned the observed event counts in each category.

	radar observing rain	radar observing no-rain
satellite estimate giving rain	<i>a</i>	<i>b</i>
satellite estimate giving no-rain	<i>c</i>	<i>d</i>

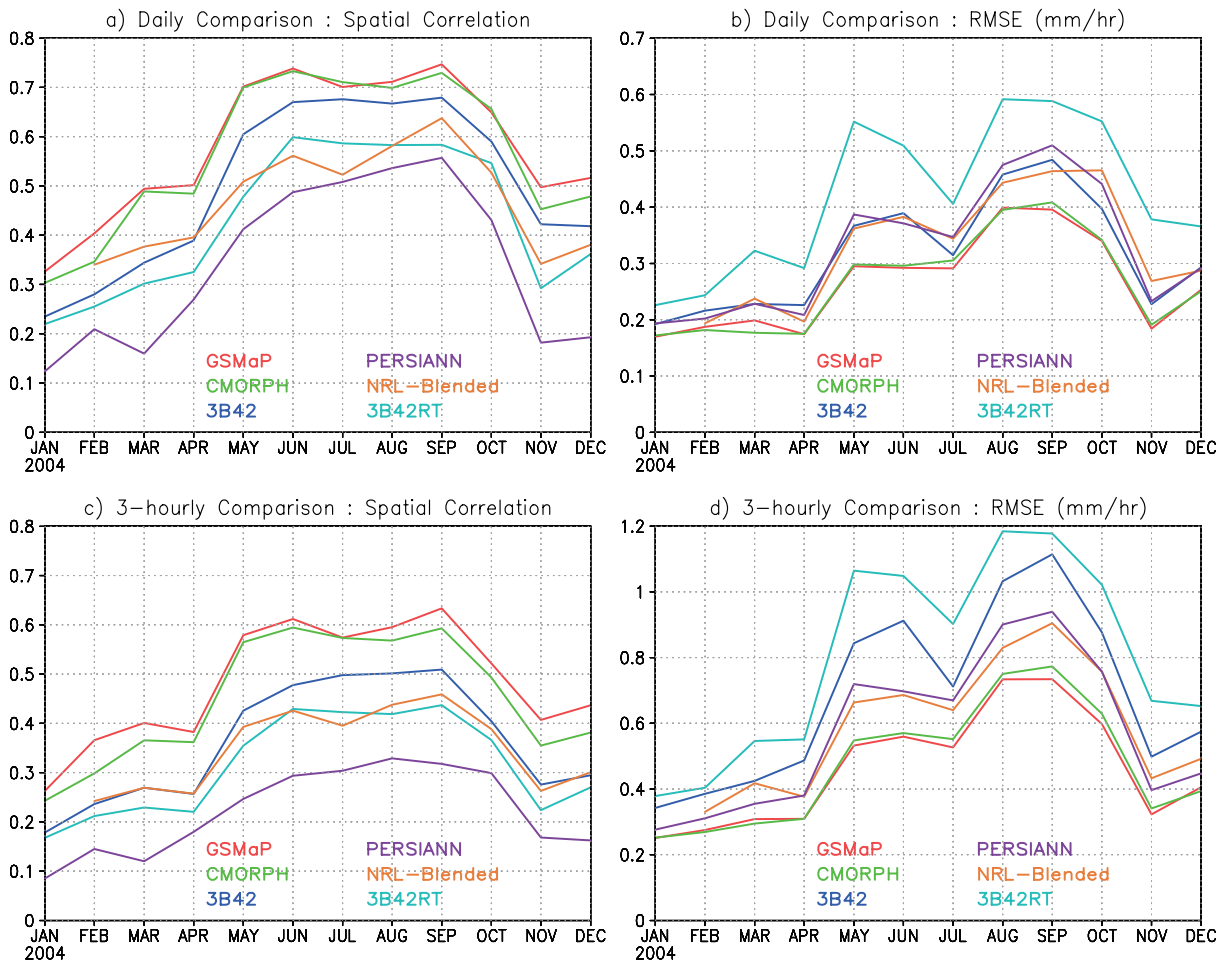


Fig. 4. Time series of radar validation for January through December 2004 using estimates in terms of (a), (c) spatial correlation coefficients and (b), (d) RMSEs. Daily estimates are analyzed in Figs. (a) and (b), and 3-hourly estimates are analyzed in (c) and (d). Monthly averaged statistics are displayed in the panels. Lines for the satellite data are the same as in Fig. 3. The horizontal resolution of the datasets is $0.25^\circ \times 0.25^\circ$ latitude/longitude.

observed raining events. A further description of the statistics was given by Wilks (2006). Statistics were computed for daily, 3-hourly, or hourly estimates and averaged monthly.

The radar dataset is a 1-hour accumulation dataset from a collection of instantaneous scans, while a satellite estimate is based on instantaneous observation. Rain areas of 1-hour accumulation data tend to be slightly larger than those of instantaneous data because rainfall areas propagate within an hour. Thus, the POD and FB are expected to be slightly smaller using the radar data rather than the instantaneous verification dataset, while the FAR is rather reliable.

This is less effective for estimates averaged over longer time-scales. In practice, satellite estimates have large errors, owing to their algorithms. Therefore, this paper focuses on validations of the algorithms.

Surface-type information is from the land-sea database of the TRMM Science Data and Information System (TSDIS) toolkit, a software library of functions provided for TRMM science algorithm developers.

3. Comparisons between various satellite estimates

This section compares six satellite estimates from

various national centers and universities with the radar data. Figure 3 plots a monthly series of the radar data and the satellite-based estimates averaged in the analyzed area. In this area, rainfall amounts were large in May through June, as a result of two typhoon landfalls and the stationary Baiu front, and in August through October, as a result of seven typhoon landfalls and the stationary Akisame front, in addition to contributions by extratropical cyclones. The variation in 3B42 data, which was adjusted by gauge information, corresponded well to that in the radar data. The 3B42RT data were overestimated, while other data were underestimated, based on radar data. Figures 4 and 5 plot time series of radar validation for January through December 2004, with statistics averaged for each month. The statistics were computed using 3-hourly estimates for Figs. 4c and d, or daily averaged estimates for the other figures, with a horizontal resolution of $0.25^\circ \times 0.25^\circ$ latitude/longitude. In Fig. 4a for daily comparison, spatial correlation coefficients were high during the boreal summer and low during the boreal winter. Performances of satellite estimates tended to be better during the warm season, which was consistent with validation results for the United States (Gottschalck et al. 2005; Ebert et al. 2007) and Australia (Ebert et al. 2007), in addition to results of the PIP-3 (Adler et al. 2001). The correlation coefficients (RMSEs) of GSMaP and CMORPH were higher (smaller) than those of the other products. RMSEs were large in the 3B42RT data, while those of the 3B42 data, which were adjusted by gauges, were smaller than the 3B42RT RMSEs.

Figures 4c and d present the results for 3-hourly estimates; they exhibit features similar to those of Figs.

Figures 4c and d present the results for 3-hourly estimates; they exhibit features similar to those of Figs.

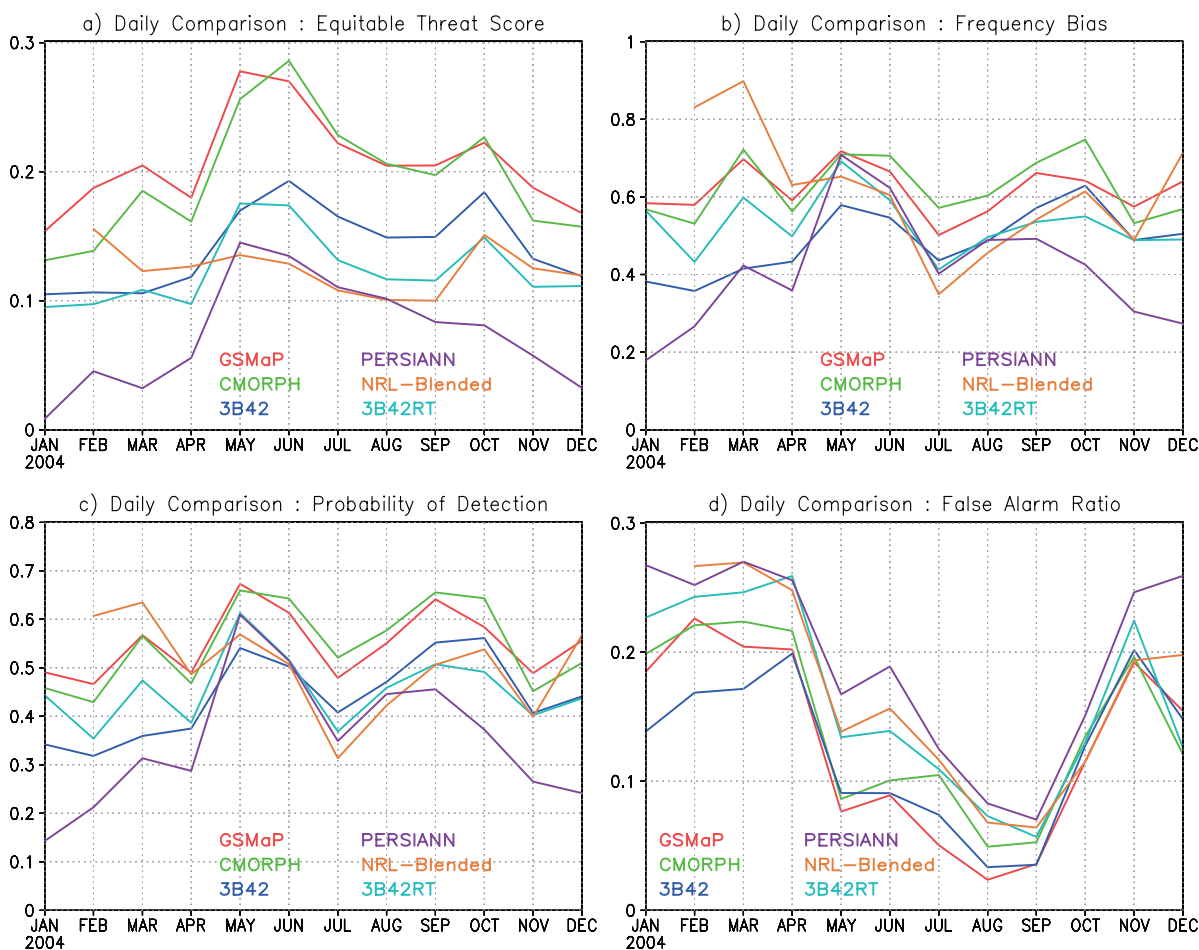


Fig. 5. Same as Fig. 4 for daily estimates, except that (a) ETS, (b) FB, (c) POD, and (d) FAR are presented.

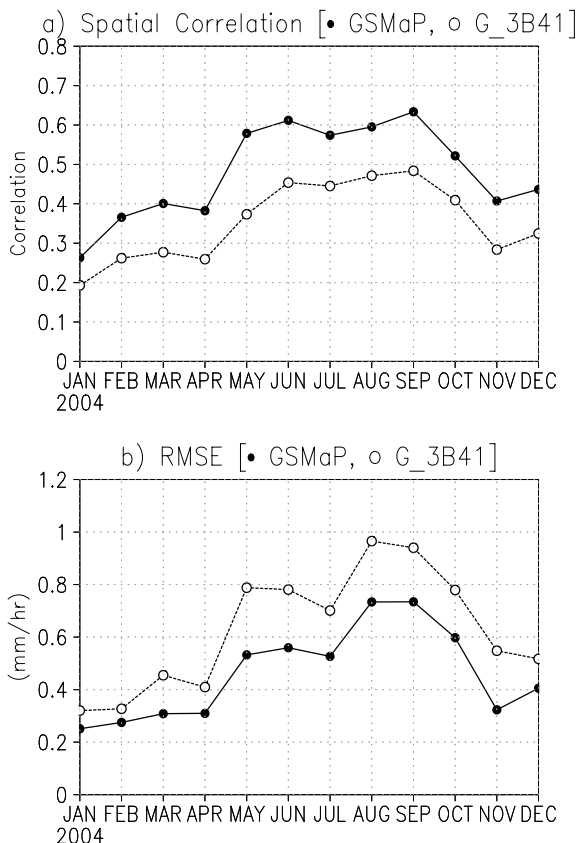


Fig. 6. Time series of radar validation for 3-hourly estimates of GSMaP and G_3B41 data. Monthly averaged (a) spatial correlation coefficients and (b) RMSEs are displayed in the panels. Dots denote GSMaP data, and open circles denote G_3B41 data.

4a and b. The correlation coefficients were lower than those in Fig. 4a, and the RMSEs were larger than those in Fig. 4b. This result indicates that the 3-hourly satellite estimates were not as accurate as the daily estimates. For the 3-hourly estimates, the results provided by GSMaP and CMORPH were better than those of the other products, which were the same as for the validation results of daily estimates.

Figure 5 presents the 2 × 2 contingency table statistics. The ETS indicates similar but noisy features in the correlation. The FB indicates underestimation of rain areas in the satellite estimates. Case studies revealed that these underestimates were largely related to mistaken rain detection, probably due to algorithm problems, and it seems that the differences in the orig-

inal instantaneous and 1-hour accumulation data were not very influential in daily estimates, as noted in Section 2. The POD values of GSMaP and CMORPH tended to be higher than for the other products. The FAR values were higher during the cold season than during the warm season, indicating that false rainfall was found in the satellite estimates more frequently. The FAR values of the 3B42 data adjusted by the gauges were relatively small, especially during the boreal winter.

The superiority of GSMaP and CMORPH could be related to the temporal interpolation of the PMW estimates based upon the morphed technique. Figure 6 clearly demonstrates this in the validation results of 3-hourly GSMaP and G_3B41 estimates. Here, the GSMaP and G_3B41 procedures were the same, except for the IR interpolation method. Correlation coefficients for GSMaP were 0.2 higher than those for G_3B41, and the RMSEs of the GSMaP were smaller than those of the G_3B41. Thus, the IR interpolation method can contribute significantly to differences in validation results, as indicated in Figs. 4 and 5.

In the above analyses, a threshold of 0.0 mm day⁻¹ was used to discriminate between rain (above 0.0 mm day⁻¹) and no rain (0.0 mm day⁻¹). For validation of rainfall above specific rain rates, four thresholds (1.0, 5.0, 10.0, and 20.0 mm day⁻¹) were tested. The results are plotted in Fig. 7 for the ETS, using daily estimates for six rainfall products. High values of ETS were found for moderate thresholds (1 to 5 mm day⁻¹) during the warm season for all products, including the gauge-adjusted 3B42. This result indicates that satellite estimates are poor for light rainfall during the warm season. The ETS values, excluding light rainfall for the 3B42, are comparable to those for the GSMaP and CMORPH, while the ETS values for all data of the 3B42 are lower (Fig. 5a). The direct conversion from the IR Tbs to the rain rates in the TMPA method could have been strongly affected by a weak relationship between rain intensity and cloud top temperature for light rainfall. For all products, ETS values for the threshold of 20.0 mm day⁻¹ were lower than those for the thresholds of 1.0 or 5.0 mm day⁻¹. This result suggests that their performances were poor in very heavy rainfall. A possible reason will be discussed in Section 5.

4. Comparison between GSMaP products

This section compares GSMaP satellite estimates with radar data. Further analyses were performed in terms of data sources, techniques, and surface types

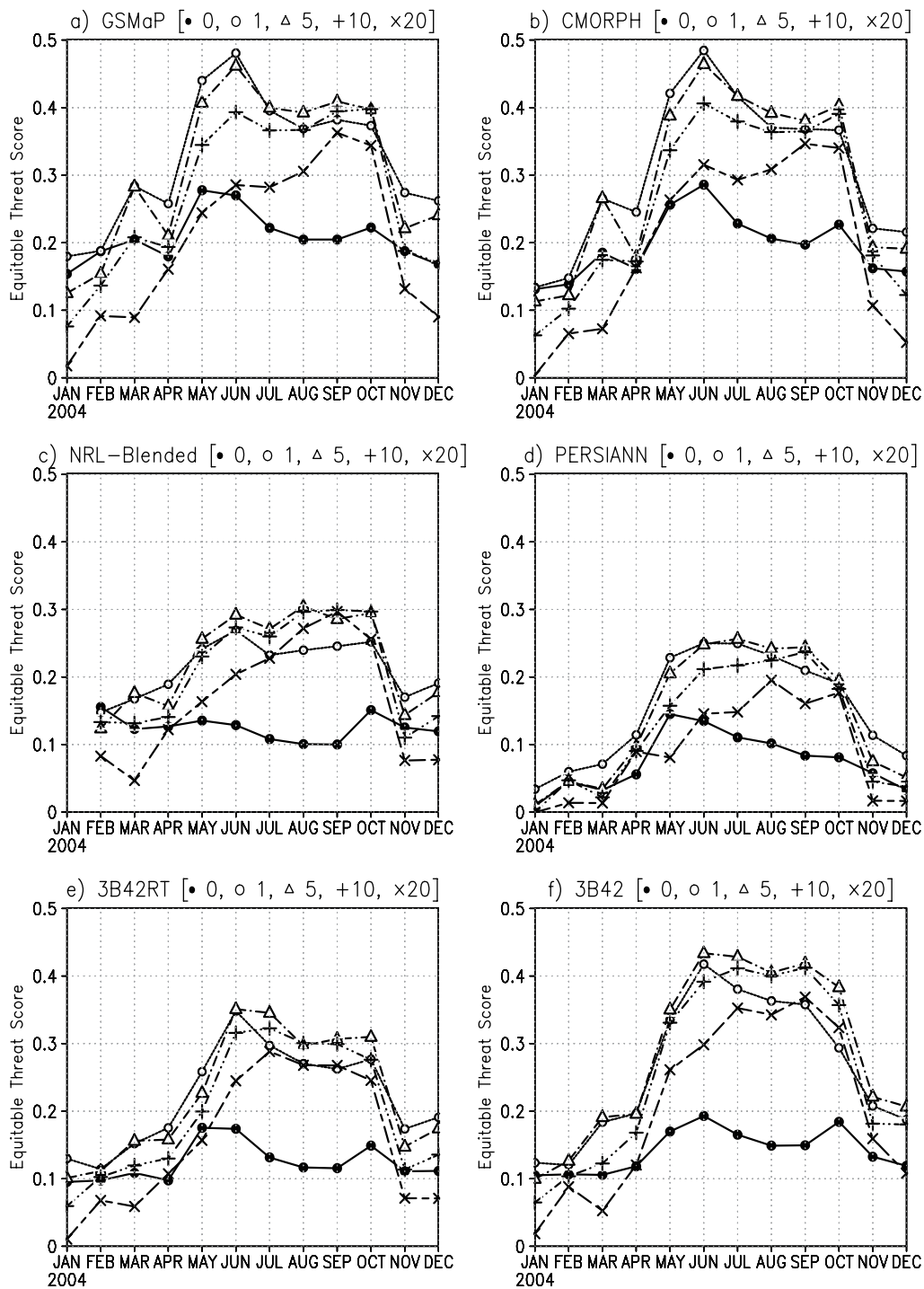


Fig. 7. Time series of the ETS using daily estimates in terms of (a) GSMaP, (b) CMORPH, (c) NRL-Blended, (d) PERSIANN, (e) 3B42RT, and (f) 3B42 data. Monthly averaged statistics are displayed in the panels. Open circles denote results for a threshold of 1.0 mm day⁻¹, triangles denote results for a threshold of 5.0 mm day⁻¹, pluses denote results for a threshold of 10.0 mm day⁻¹, and crosses denote results for a threshold of 20.0 mm day⁻¹. Dots are the same as in Fig. 5a (i.e., a threshold of 0.0 mm day⁻¹). The horizontal resolution of the datasets is 0.25° × 0.25° latitude/longitude.

to reveal their strengths and limitations.

Figure 8 plots a time series of radar validation for January through December 2004, with statistics averaged for each month. The statistics were computed using daily averaged estimates with a horizontal resolution of $0.25^\circ \times 0.25^\circ$ latitude/longitude. The results from G_MWI, which was based on only retrievals of the PMW imagers, had the worst correlation, RMSE, and POD, and the best FAR. The POD results revealed that rainfall detection was poor, due to sampling errors by the PMW imagers. Such sampling errors, which have been discussed in many papers (e.g., Bell and Kundu 1996, 2000), could have led to poor correlations and RMSEs. However, the PMW imagers were able to measure the emission signals from the precipitation, and false signals of rainfall were less frequent, as revealed in the results for the FAR. Moreover, GSMaP performed slightly better than G_IVK (Fig. 8). As demonstrated by Ushio et al. (2009), a longer time after the last microwave satellite overpass led to larger errors in estimates using the morphed technique.

Furthermore, differences among the sensors were examined in hourly estimates. In the GSMaP algorithm, the PMW imagers, PMW sounders, and GEO

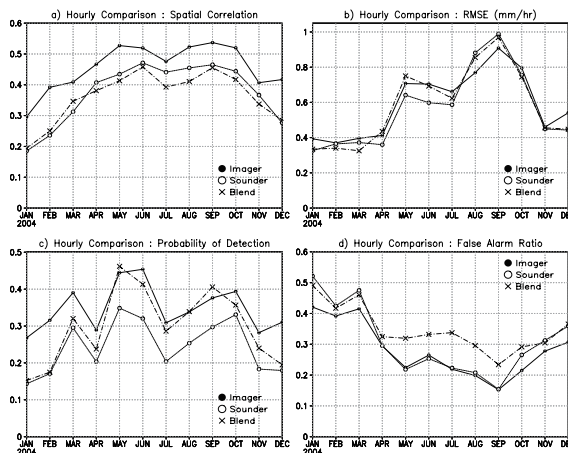


Fig. 9. Time series of validation over the ocean using hourly estimates of the GSMaP data for different satellite sensors. Monthly averaged statistics are displayed in the panels. Dots denote the PMW imager, open circles denote the PMW sounder, and crosses denote the blend of the PMW-IR sensors. The horizontal resolution of the datasets is $0.1^\circ \times 0.1^\circ$ latitude/longitude.

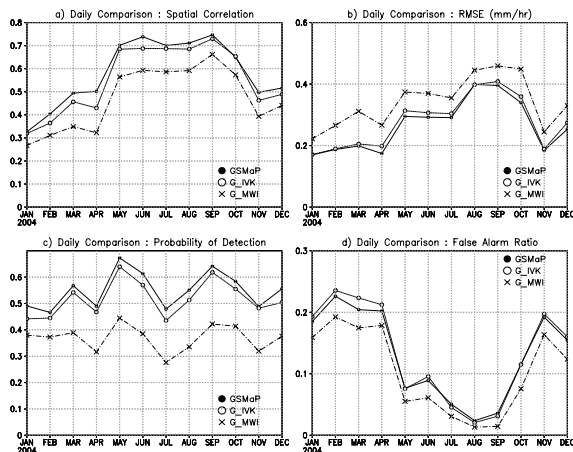


Fig. 8. Time series of radar validation using daily estimates in terms of (a) correlation coefficient, (b) RMSE, (c) POD, and (d) FAR. Monthly averaged statistics are displayed in the panels. Dots denote GSMaP data; open circles denote G_IVK data; and crosses denote G_MWI data. The horizontal resolution of the datasets is $0.25^\circ \times 0.25^\circ$ latitude/longitude.

IR radiometers were used as data sources, with consideration of differences in the sensor datasets noted in Section 2.2. To quantify the effects, validation using radar data was performed over the ocean for each sensor. Figure 9 presents the results for different data sources using hourly estimates of the GSMaP with a horizontal resolution of $0.1^\circ \times 0.1^\circ$ latitude/longitude. An estimate denoted as a “blend” was computed by the GSMaP blended PMW-IR algorithm in areas with no overpass of the microwave sensors, and this estimate was quite different from a direct estimate of the IR data. Sampling problems as shown in analyses of Fig. 8 are not related here because Fig. 9 presents results of hourly validations. Three kinds of satellite estimates in the analysis of Fig. 9 corresponded to simultaneously different areas among them, and comparisons of averages of the statistics became meaningful.

Overall, results for the PMW imagers were better than those for the other data sources. Because microwave emission and scattering were more directly related to precipitation than to cloud-top temperature from the IR observation, the PMW algorithms generally provided more accurate instantaneous rainfall estimates than the IR algorithms did (Ebert et al. 1996;

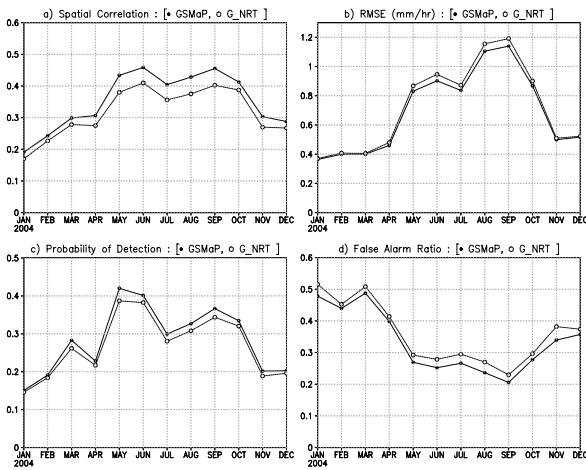


Fig. 10. Differences in validation results using hourly estimates of GSMaP and GSMaP_NRT data. The panels are the same as in Fig. 9, except that all surface types are presented. Dots denote GSMaP results, and open circles denote GSMaP_NRT results.

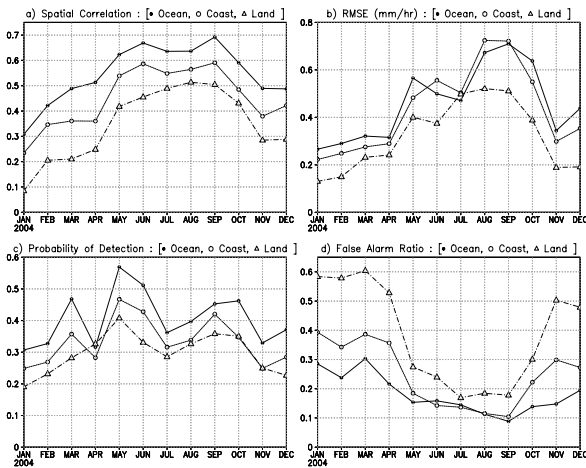


Fig. 11. Time series of radar validation for GSMaP data for January through December 2004 using 3-hourly estimates in terms of (a) correlation coefficient, (b) RMSE, (c) POD, and (d) FAR. Monthly averaged statistics are displayed in the panels. Dots denote ocean, open circles denote coast, and triangles denote land. The horizontal resolution of the datasets is $0.25^\circ \times 0.25^\circ$ latitude/longitude.

Smith et al. 1998). Correlation coefficients for estimates using the PMW imagers were 0.1 higher than those for estimates using the PMW sounders and the blend of PMW-IR sensors. Correlation coefficients for the PMW sounders were slightly higher than those for the blend of PMW-IR sensors. The POD values for the PMW sounders were relatively low, while the FAR values were also low. This result was consistent with results for the algorithm developed by NOAA based upon scattering information of the PMW sounders. The AMSU-B had high-frequency channels with good

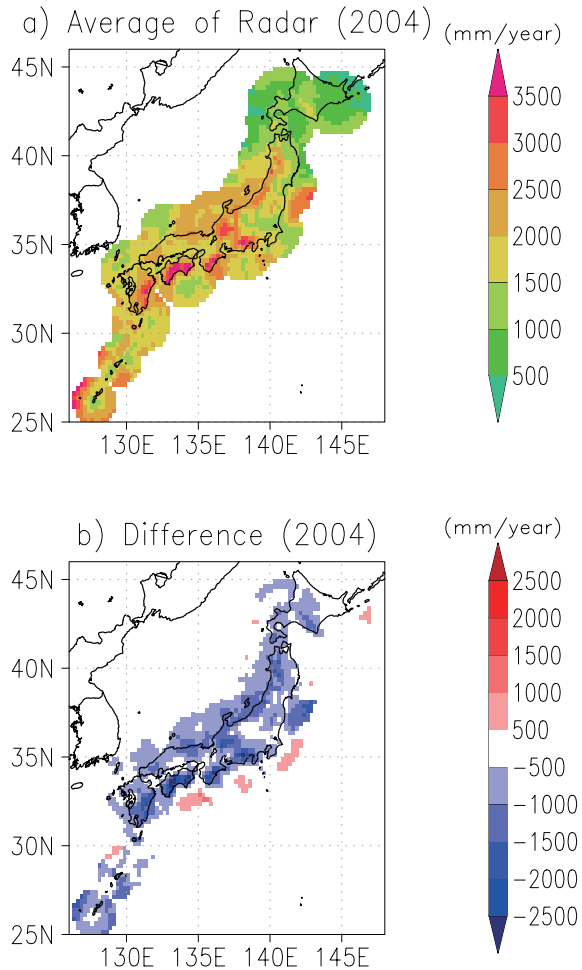


Fig. 12. (a) Averages of the radar data during 2004 and (b) differences between the GSMaP and the radar (i.e., GSMaP minus radar), averaged during 2004. The horizontal resolution of the datasets is $0.25^\circ \times 0.25^\circ$ latitude/longitude.

sensitivity to rainfall involving ice particles above the freezing level, and poor sensitivity to shallow rainfall. Thus, the results demonstrated less detection and fewer false signals of over-ocean rainfall by the PMW sounders. Over land, estimates from the PMW sounders were equivalent to those from the PMW imagers in terms of scattering-based methods, as described in Section 2.2. These results demonstrated that effective performance by merges of PMW sounders was verified over ocean, due to less false rainfall with the PMW sounders.

In the GSMaP PMW-IR blended algorithm, rainfall features were propagated via IR data both forward and backward in GSMaP, while they were only propagated forward in G_NRT, the merit of which was a faster processing time. The relationship between GSMaP and G_NRT was similar to that between CMORPH and QMORPH of the NOAA CPC. Differences in validation results for GSMaP and G_NRT are indicated in Fig. 10. Owing to the inclusion of backward processes in GSMaP, the GSMaP results were better than the G_NRT results. Differences between correlations and RMSEs were larger during the boreal summer than during the boreal winter, due to short-lived convection during summer and rainfall associated with typhoons between June and October. Differences in the POD were large in the warm season, while differences in the FAR were nearly constant throughout the year, suggesting that relatively low detection of rainfall using G_NRT was more apparent during warm seasons. These results implied that these differences would be larger in the tropics, where short-lived convection was observed frequently.

Differences in validation results were examined by surface type. Figure 1a reveals surface-type distributions over the analyzed area. Note that the grid points of “land” (green in the figure) were located in the mountainous regions in Japan, as seen in the topographic data of Fig. 1b from the GTOPO30 dataset (Row et al. 1995) provided by the United States Geological Survey. Figure 11 presents time series of radar validation for GSMaP over ocean, coast, and land, with statistics averaged for each month. The statistics were computed for 3-hourly estimates with a horizontal resolution of $0.25^\circ \times 0.25^\circ$ latitude/longitude. The spatial correlation indicated distinct seasonal variations for all surface types. Overall, results over the ocean had the best correlation, and results over mountainous regions (land) had the worst. This result was closely related to ocean algorithms that used the low-frequency channels of the PMW imagers, since

the algorithms for the PMW imagers differed for different surface types as noted in Section 2.2. Kubota et al. (2007) found a similar seasonal variation in the validation results of retrievals from the TMI for different surface types around Japan. The FAR indicated that false rainfall is found over mountainous regions more often in the boreal winter, which is closely related to the rain/no-rain identification problem of the PMW algorithm for snow-covered land.

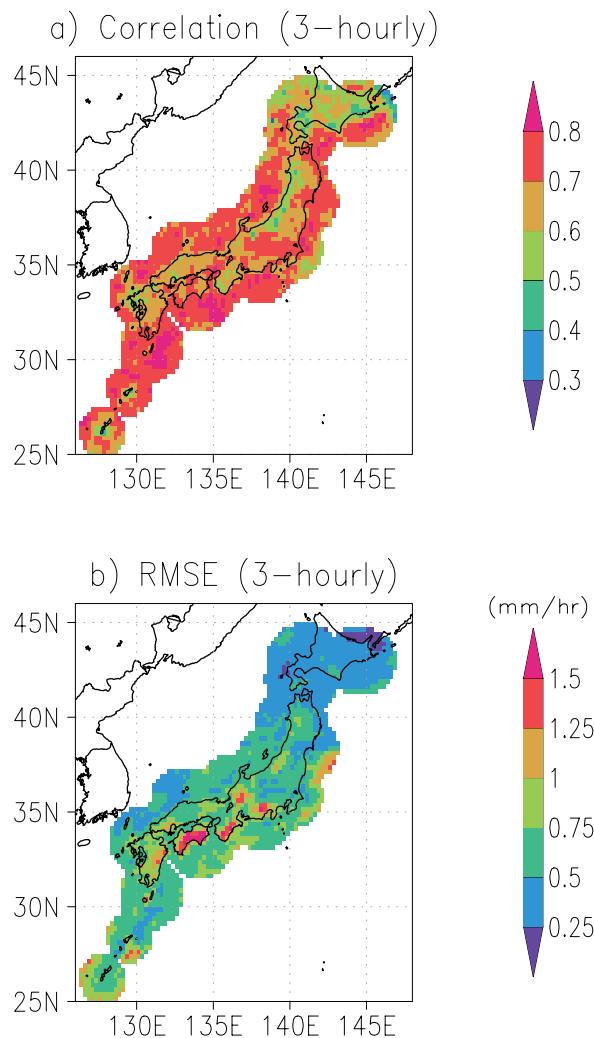


Fig. 13. (a) Temporal correlation and (b) RMSE between 3-hourly estimates of the radar and GSMaP data for January through December 2004. The horizontal resolution of the datasets is $0.25^\circ \times 0.25^\circ$ latitude/longitude.

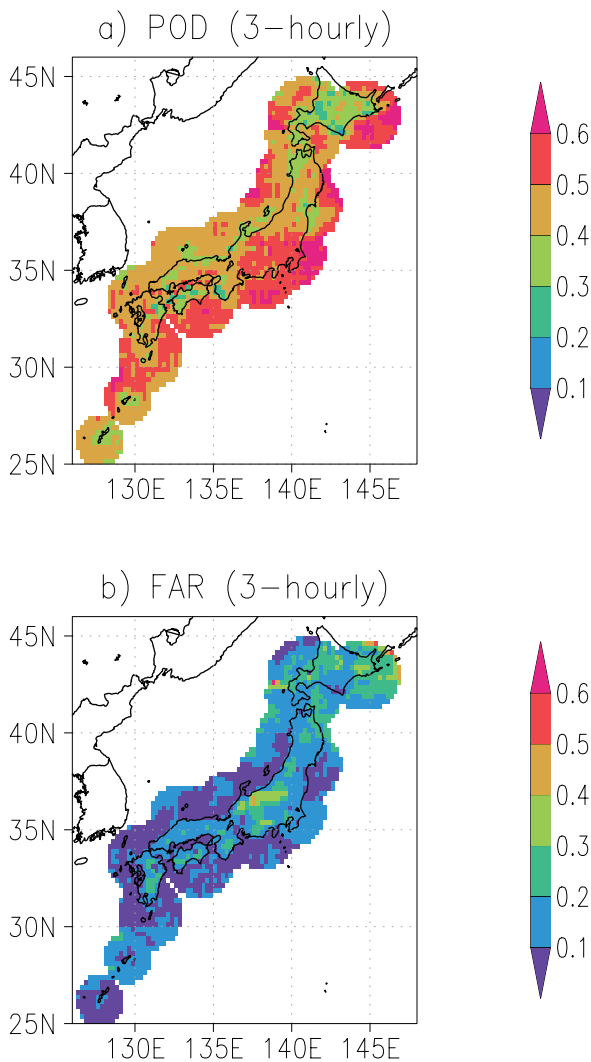


Fig. 14. Same as Fig. 13, except that POD and FAR are presented.

The previous validation in this paper was made for spatial evaluations. Here, temporal variations with individual pixels of $0.25^\circ \times 0.25^\circ$ latitude/longitude were analyzed using 3-hourly estimates for January through December 2004. Figure 12a depicts rain rates of the radar, averaged during 2004. Note that a threshold of the temperature was used in this study for analysis of non-snowfall areas, as described in Section 2.3. Heavy rainfall was found in the south of Shikoku Island (133°E , 33°N), the southeast of Kii Peninsula (135.5°E , 33.5°N), and the southern slopes of the Akaishi Mountains (138°E , 35°N). These regions are well-known for their frequently heavy orographic

rainfall associated with warm, moist southeasterly winds at low altitude. When the air flowing over rugged terrain is potentially unstable, the lifting induced by the terrain can lead to the formation of orographic clouds of cumuli or cumulonimbi, which can be very important precipitation producers (cf., Houze 1993). Figure 12b depicts differences between the GSMaP and the radar data. Large negative values below $1500 \text{ mm year}^{-1}$ found in areas with heavy orographic rainfall indicate underestimation of the GSMaP there, which will be discussed in the next section. Positive values over the ocean could be closely related to a tendency of the PMW retrievals. Kubota et al. (2007) demonstrated that TMI retrievals of the GSMaP tended to be larger than those of the PR 2A25 (Iguchi et al. 2000; Iguchi 2007) over the mid-latitudes during boreal winter.

Temporal correlation and RMSE results for GSMaP are presented in Fig. 13, and POD and FAR results are presented in Fig. 14. Here, signals at the boundaries of radar observation areas over the ocean may have had radar problems, as noted in Section 2.2. Relatively high temporal correlation coefficients were found over the ocean, and only the ocean had correlations above 0.8 (Fig. 13a). Low correlations below 0.6 were scattered over coasts, such as Okinawa Island (128°E , 26.5°N) and the northern coast of Kyusyu Island (129.5°E , 33°N). The POD values were below 0.4 over these islands (Fig. 14a). This is related to a rain/no-rain identification problem of the PMW algorithm over coasts. The PMW algorithm of the GSMaP Project used a modification of the McCollum and Ferraro (2005) method (Kubota et al. 2007). However, as discussed in McCollum and Ferraro (2005), the PMW footprint over coasts is a mixture of radiometrically cold ocean and radiometrically warm land surfaces, and the performances of the algorithms are worse over coasts than over land and ocean. Moreover, correlations below 0.6 are found in coastal areas (37°N to 40°N) in the Sea of Japan, and are closely related to mesoscale convective systems observed frequently during winter. For Hokkaido Island (141°E , 43°N), the correlations below 0.6 were related to the low POD values in Fig. 14a. Because the FAR was relatively low for Hokkaido Island, the screening of snow cover resulted in rain detection errors for the rain/no-rain identification method. Large RMSE values (Fig. 13b) were found for coastal areas with frequently heavy orographic rainfall. In Fig. 14b, the large FAR values found for the Hida Mountains (138°E , 36.8°N) were related to false rainfall due to snow cover. The large

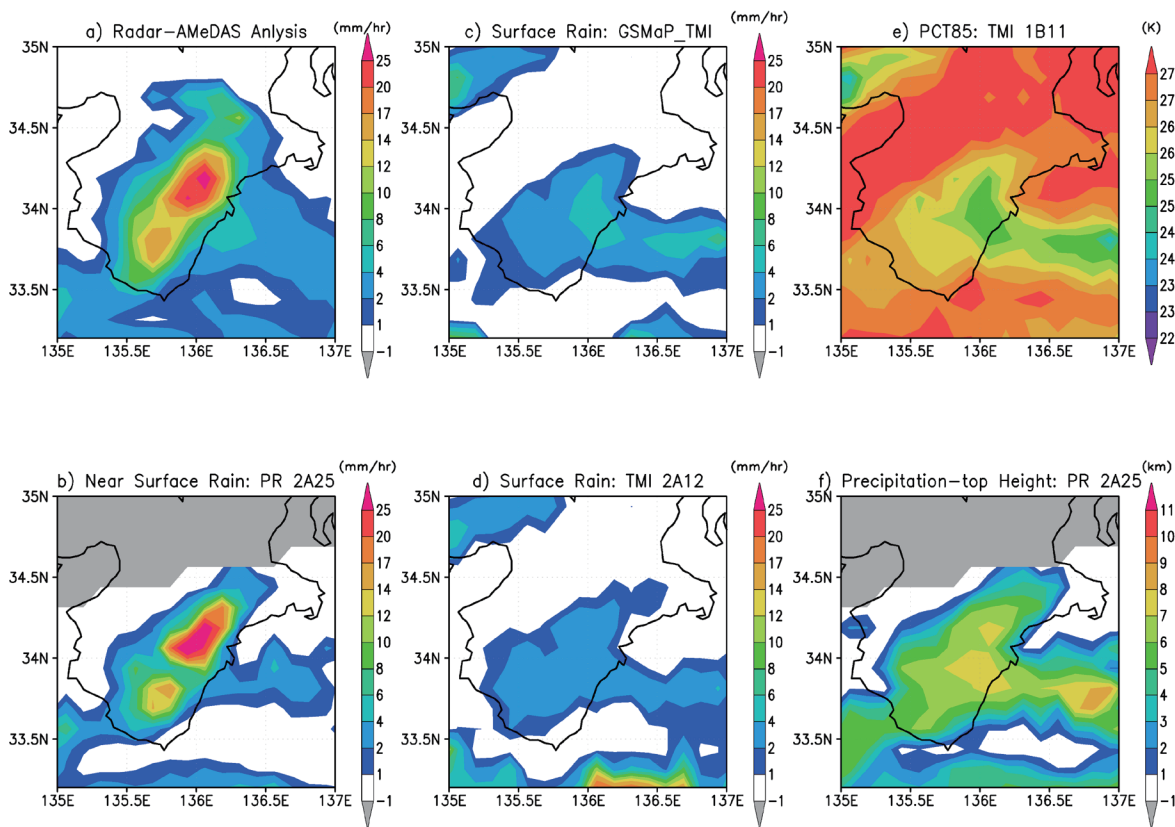


Fig. 15. Case study of orographic rainfall over Kii Peninsula on July 30, 2004. The spatial resolution of all panels is $0.125^\circ \times 0.125^\circ$ latitude/longitude. (a) ground-based radar data, (b) PR 2A25 near-surface rain rate (mm h^{-1}), (c) GSMaP_TMI surface rain (mm h^{-1}), (d) TMI 2A12 surface rain (mm h^{-1}), (e) TMI PCT85 (K), (f) PR 2A25 precipitation-top height (km). The observation time of the ground-based radar was 15:00 to 15:59Z, that of PR was 15:34Z, and that of TMI data was 15:33Z (TRMM orbit number: 38228).

FAR values also found for the ocean east of Hokkaido Island were related to false rainfall due to sea ice.

5. Discussion

Large errors of the GSMaP were found in areas with frequently heavy orographic rainfall over the Japanese Archipelago. One reason for these errors was the relatively low POD values (Fig. 14a), due to the rain/no-rain identification problem over coasts. However, the identification problem over coasts was usually problematic for weak rainfall with a small Tb depression due to scattering. Another reason could be related to heavy rainfall. We focused on hydrometeor vertical profiles for orographic rainfall, which were influential in the PMW retrievals. Figure 15 presents a case study of orographic rainfall over the Kii Peninsula on July 30, 2004. The spatial resolu-

tion of all panels in Fig. 15 is $0.125^\circ \times 0.125^\circ$ latitude/longitude. In this case, strong easterly winds above 10 m s^{-1} , associated with Typhoon Namtheun, were observed from 12:00UTC July 30 to 01:00UTC July 31 in surface meteorological data at Owase (136°E , 34°N), where mountains higher than 500 m are very close to the coastline running northeast to southwest (Figs. 1b and 16a). In the ground-based radar data (Fig. 15a) and the PR 2A25 Version 6 data (Fig. 15b), large surface rain rates above 25 mm h^{-1} were detected around Owase at 15:00UTC on July 30. Large surface rainfall events, such as those seen in radar observations, were not detected for the two products for which surface rain rates were retrieved from the TMI data, which observed simultaneously with the PR. The TMI retrievals were produced by the GSMaP algorithm (GSMaP_TMI) (Fig. 15c) and the 2A12 Version 6 by

the GPROF algorithm (Fig. 15d). In both algorithms, surface rain rates over land were computed based on observed Tbs at 85.5 GHz. Figure 15e presents polarization-corrected temperatures at 85.5 GHz (PCT85) defined by Spencer et al. (1989). The pattern for PCT85 was more similar to that of the precipitation-

top height presented in Fig. 15f than the 2A25 surface rain rates. A similar relationship between PCT85 and the precipitation-top height was reported by Kubota et al. (2007) for a mesoscale convective system over western Africa. For the present study, the precipitation-top height was defined as the top bin above 0.3 mm h^{-1} in 2A25. Depressions of PCT85 over orographic rainfall around Owase were similar to those over the ocean east of Owase, the PR rainfall intensities of which were weak. According to the PCT85 pattern, GSMaP_TMI and 2A12 surface rain rates were weak for the orographic rainfall around Owase and the ocean east of Owase.

In a case study of heavy rain in the Owase area using range height indicator (RHI) radar data, Takeda and Takase (1980) demonstrated continuous rain originating from mid-level clouds and a remarkable increase in radar echo intensity with decreasing height below the bright band when an easterly wind was prevalent. Figure 16b depicts a vertical cross section of precipitation along the track of the PR for the orographic rainfall around Owase. At 12:00UTC on July 30, the freezing level height was 5.2 km from the JMA GANAL. A large increase in rain rates was observed below the freezing level, and rain rates above 80 mm h^{-1} were observed in the heavy rainfall area. In contrast, these features were not found over the ocean (Fig. 16c), while precipitation top heights around 0.3 mm h^{-1} (Fig. 16c) were similar to those in Fig. 16b. Thus, PMW scattering associated with ice particles above the freezing level was relatively weak in the orographic heavy rainfall, and retrieval using high-frequency channels could be regarded as small. Underestimation of rainfall by the PMW algorithms was closely related to the large errors in areas of orographic rainfall. This result also implied that the same features for orographic heavy rainfall could be found outside Japan (e.g., in moist monsoonal regions such as South Asia).

6. Summary

Six high-resolution satellite rainfall estimates were compared with ground-based radar data (JMA Radar-AMeDAS precipitation analysis) as a reference for January through December 2004 over regions with surface temperatures above 4°C . For 3-hourly or daily averaged estimates with a horizontal resolution of $0.25^{\circ} \times 0.25^{\circ}$ latitude/longitude, radar validation results tended to be better during the boreal summer and worse during the boreal winter. The validation results of GSMaP and CMORPH, which used the tem-

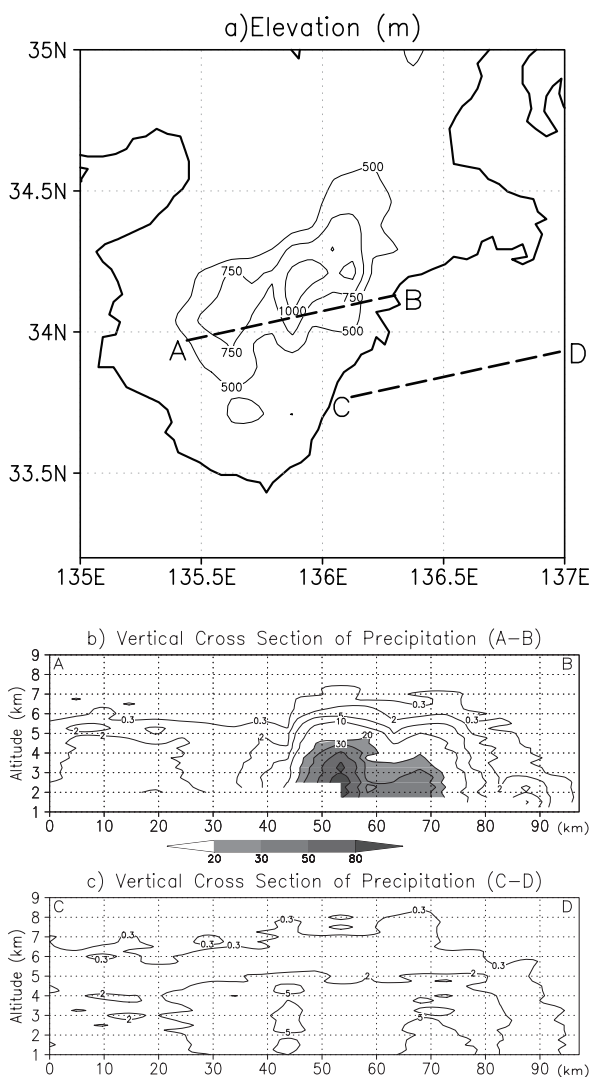


Fig. 16. (a) Elevation map of Kii Peninsula area. (b) Vertical cross section of precipitation by TRMM/PR for the same case as in Fig. 15 over the A-B segment of Fig. 16a. (c) Same as (b), except over the C-D segment of Fig. 16a. The unit in (b) and (c) is mm h^{-1} . Rain rates above 20 mm h^{-1} are shaded.

poral interpolation based on the morphed technique using GEO IR information, were better than those of other products. Satellite estimates were poor for light rainfall during the warm season and for very heavy rainfall.

Further analyses of satellite estimates were performed in terms of data sources and surface types to determine their strengths and limitations. The rainfall estimates over the ocean were more efficient using PMW sounders in addition to PMW imagers. This finding is related to less false rainfall being detected by the PMW sounders. Overall, validation results over the ocean were best, and results over mountainous regions were worst. Rainfall estimates were poor over coasts and small islands, due to the rain/no-rain identification problem over coasts. Heavy rainfall during 2004 was located in areas with frequent orographic heavy rainfall over the Japanese Archipelago, and large errors in satellite estimates were detected there. This result could be closely related to issues of hydrometeor vertical profiles in the PMW retrievals, related to the poor satellite estimates in very heavy rainfall.

In this study, the analyzed period was limited to one year, and one of the merits for the year 2004 was a constant number of instruments. A sampling issue is involved in choosing a single year over multiple years, and results of longer periods may be desired. This study compared satellite rainfall estimates with reference to a ground radar dataset calibrated by rain gauges. However, the calibration of the radar by gauges is uncertain over the ocean, and results may be unreliable there. Satellite estimates are validated for non-snowfall regions, and validations of snowfalls are beyond the scope of this study. This issue has been left for future work.

Acknowledgments

This study is supported by the Global Satellite Mapping of Precipitation (GSMaP) Project under the JST-CREST, and by the Mitsui & Co., Ltd. Environment Fund. The GSMaP Project website is <http://www.radar.aero.osakafu-u.ac.jp/~gsmap/>. The authors would like to thank Dr. K. Aonashi and Mr. H. Eito (Meteorological Research Institute, Japan Meteorological Agency) and Dr. T. Iguchi (National Institute of Information and Communications Technology) for their valuable comments, and D. Katagami, T. Watanabe and H. Ashiwake (Osaka Prefecture University) for helpful computing assistance. They also thank the editor and the anonymous reviewers for their valuable comments. The dataset

of the Radar-AMeDAS Precipitation Analysis was provided by the Japan Meteorological Agency. The IPWG website (<http://www.isac.cnr.it/~ipwg/IPWG.html>) and the PEHRPP website (<http://essic.umd.edu/~msapiano/PEHRPP/>) provided information on precipitation products.

References

- Adler, R. F., C. Kidd, G. Petty, M. Morissey, and H. M. Goodman, 2001: Intercomparison of Global Precipitation Products: The Third Precipitation Intercomparison Project (PIP-3). *Bull. Amer. Meteor. Soc.*, **82**, 1377–1396.
- Aonashi, K., and G. Liu, 2000: Passive microwave precipitation retrievals using TMI during the Baiu period of 1998 Part I: Algorithm description and validation. *J. Appl. Meteor.*, **39**, 2024–2037.
- Aonashi, K., J. Awaka, M. Hirose, T. Kozu, T. Kubota, G. Liu, S. Shige, S. Kida, S. Seto, N. Takahashi, and Y. N. Takayabu, 2009: GSMaP passive microwave precipitation retrieval algorithm: Algorithm description and validation, *J. Meteor. Soc. Japan*, **87A**, 119–136.
- Arkin, P. A., J. Turk, and E. Ebert, 2005: Pilot Evaluation of High Resolution Precipitation Products (PEHRPP): A contribution to GPM planning. *Fifth Global Precipitation Mission (GPM) Planning Workshop*, Tokyo, Japan, JAXA. (Available online at <http://www.eorc.jaxa.jp/GPM/event/ws5/hp/jp/agenda.html>).
- Bell, T. L., and P. K. Kundu, 1996: A study of the sampling error in satellite rainfall estimates using optimal averaging of data and a stochastic model. *J. Climate*, **9**, 1251–1268.
- Bell, T. L., and P. K. Kundu, 2000: Dependence of satellite sampling error on monthly averaged rain rates: Comparison of simple models and recent studies. *J. Climate*, **13**, 449–462.
- Ebert, E. E., M. J. Manton, P. A. Arkin, R. J. Allam, G. E. Holpin, and A. J. Gruber, 1996: Results from the GPCP algorithm intercomparison programme. *Bull. Amer. Meteor. Soc.*, **77**, 2875–2887.
- Ebert, E. E., J. E. Janowiak, and C. Kidd, 2007: Comparison of near-real-time precipitation estimates from satellite observations and numerical models. *Bull. Amer. Meteor. Soc.*, **88**, 47–64.
- Ferraro, R. R., F. Weng, N. Grody, L. Zhao, H. Meng, C. Kongoli, P. Pellegrino, S. Qiu, and C. Dean, 2005: NOAA operational hydrological products

- derived from the AMSU, *IEEE Trans. Geosci. Remote Sens.*, **43**, 1036–1049.
- Gottschalck, J., J. Meng, M. Rodell, and P. Houser, 2005: Analysis of multiple precipitation products and preliminary assessment of their impact on Global Land Data Assimilation System land surface states. *J. Hydrometeorol.*, **6**, 573–598.
- Grody, N. C., 1991: Classification of snow cover and precipitation using the special sensor microwave imager. *J. Geophys. Res.*, **96**, 7423–7435.
- Haddad, Z., E. A. Smith, C. D. Kummerow, T. Iguchi, M. R. Farrar, S. L. Durden, M. Alves, and W. S. Olson, 1997: The TRMM "day-1" radar/radiometer combined rain-profiling algorithm. *J. Meteor. Soc. Japan*, **75**, 799–809.
- Hong, Y., R. F. Adler, A. Negri, and G. J. Huffman, 2007: Flood and landslide applications of near real-time satellite rainfall estimation, *Nat. Hazards*, **43**, 285–1680.
- Houze, R. A. Jr., 1993: *Cloud Dynamics*, Academic Press, New York, 573 pp.
- Hsu, K., X. Gao, S. Sorooshian, and H. V. Gupta, 1997: Precipitation estimation from remotely sensed information using artificial neural networks. *J. Appl. Meteor.*, **36**, 1176–1190.
- Huffman, G. J., R. F. Adler, D. T. Bolvin, G. Gu, E. J. Nelkin, K. P. Bowman, Y. Hong, E. F. Stocker, and D. B. Wolff, 2007: The TRMM multi-satellite precipitation analysis: Quasi-global, multi-year, combined-sensor precipitation estimates at fine scale. *J. Hydrometeorol.*, **8**, 38–55.
- Iguchi, T., 2007: Space-borne radar algorithms. *Measuring precipitation from space EURLAINSAT and the future*, Springer, 199–212.
- Iguchi, T., T. Kozu, R. Meneghini, J. Awaka, and K. Okamoto, 2000: Rainprofiling algorithm for the TRMM Precipitation Radar. *J. Appl. Meteor.*, **39**, 12, 2038–2052.
- Joyce, R. J., J. E. Janowiak, P. A. Arkin, and P. Xie, 2004: CMORPH: A method that produces global precipitation estimates from passive microwave and infrared data at high spatial and temporal resolution, *J. Hydrometeorol.*, **5**, 3, 487–503, 2004.
- Kawanishi, T., T. Sezai, Y. Ito, K. Imaoka, T. Takeshima, Y. Ishido, A. Shibata, M. Miura, H. Inahata, and R. W. Spencer, 2003: The Advanced Microwave Scanning Radiometer for the Earth Observing System (AMSR-E), NASDA's contribution to the EOS for global energy and water cycle studies. *IEEE Trans. Geosci. Remote Sens.*, **41**, 184–194.
- Kim, J.-H., C.-H. Ho, and C.-H. Sui, 2005: Circulation features associated with the record-breaking typhoon landfall on Japan in 2004. *Geophys. Res. Lett.*, **32**, L14713, doi:10.1029/2005GL022494.
- Kubota, T., S. Shige, H. Hashizume, K. Aonashi, N. Takahashi, S. Seto, M. Hirose, Y. N. Takayabu, K. Nakagawa, K. Iwanami, T. Ushio, M. Kachi, and K. Okamoto, 2007: Global precipitation map using satelliteborne microwave radiometers by the GSMaP project : Production and validation, *IEEE Trans. Geosci. Remote Sens.*, **45**, 2259–2275.
- Kubota, T., S. Shige, K. Aonashi, and K. Okamoto, 2009: Development of nonuniform beamfilling correction method in rainfall retrievals for passive microwave radiometers over ocean using TRMM observations. *J. Meteor. Soc. Japan*, **87A**, 153–164.
- Kummerow, C., W. Barnes, T. Kozu, J. Shiue, and J. Simpson, 1998: The Tropical Rainfall Measuring Mission (TRMM) sensor package, *J. Atmos. Oceanic Technol.*, **15**, 808–816.
- Kummerow, C., Y. Hong, W. S. Olson, S. Yang, R. F. Adler, J. McCollum, R. Ferraro, G. Petty, D.-B. Shin, and T. T. Wilheit, 2001: The evolution of the Goddard profiling algorithm (GPROF) for rainfall estimation from passive microwave sensors, *J. Appl. Meteor.*, **40**, 1801–1820.
- Makihara, Y., 2000: Algorithms for precipitation nowcasting focused on detailed analysis using radar and raingauge data. Study on the Objective Forecasting Techniques, Meteorological Research Institute, Japan, *Tech. Rep. of the Meteorological Research Institute*, **39**, 63–111.
- Makihara, Y., 2007: Steps towards decreasing heavy rain disasters by short-range precipitation and land-slide forecast using weather radar accompanied by improvement of meteorological operational activities. *Tenki*, **54**, 21–33, (in Japanese).
- Makihara, Y., N. Uekiyo, A. Tabata, and Y. Abe, 1996: Accuracy of Radar-AMeDAS precipitation. *IEICE Trans. Commun.*, **E79-B**, 751–762.
- Matsuo, T., Y. Sasyo, and Y. Sato, 1981: Relationship between types of precipitation on the ground and surface meteorological elements. *J. Meteor. Soc. Japan*, **59**, 462–476.
- McCollum, J. R., and R. R. Ferraro, 2003: The next generation of NOAA/NESDIS TMI, SSM/I, and AMSR-E microwave land rainfall algorithms, *J. Geophys. Res.*, **108**, 8382,

- doi:10.1029/2001JD001512.
- McCollum, J. R., and R. R. Ferraro, 2005: Microwave rainfall estimation over coasts. *J. Atmos. Oceanic Technol.*, **22**, 497–512.
- Nakazawa, T., 2006: Madden-Julian oscillation activity and typhoon landfall on Japan in 2004, *SOLA*, **2**, 136–139.
- Okamoto, K., T. Iguchi, N. Takahashi, K. Iwanami, and T. Ushio, 2005: The global satellite mapping of precipitation (GSMaP) project, *25th IGARSS Proceedings*, 3414–3416.
- Okamoto, K., T. Iguchi, N. Takahashi, T. Ushio, J. Awaka, S. Shige, and T. Kubota, 2007: High precision and high resolution global precipitation map from satellite data, *ISAP 2007 Proceedings*, 506–509.
- Olson, W. S., C. D. Kummerow, S. Yang, G. W. Petty, W.-K. Tao, T. L. Bell, S. A. Braun, Y. Wang, S. E. Lang, D. E. Johnson, and C. Chiu, 2006: Precipitation and latent heating distributions from satellite passive microwave radiometry. Part I: Method and uncertainty estimates. *J. Appl. Meteor.*, **40**, 702–720.
- Petty, G. W., 1994: Physical retrievals of over-ocean rain rate from multichannel microwave imagery. Part 1: Theoretical characteristics of normalized polarization and scattering indices. *Meteor. Atmos. Phys.*, **54**, 79–99.
- Row, L. W., D. A. Hastings, and P. K. Dunbar, 1995: *TerrainBase worldwide digital terrain data - Documentation manual*, CD-ROM Release 1.0. National Geophysical Data Center, Boulder, Colorado.
- Shinpo, A., 2001: Radar-AMeDAS precipitation analysis (1). *Tenki*, **8**, 59–63, (in Japanese).
- Smith, E. A., J. E. Lamm, R. F. Adler, J. Alishouse, K. Aonashi, E. Barrett, P. Bauer, W. Berg, A. Chang, R. Ferraro, J. Ferriday, S. Goodman, N. Grody, C. Kidd, D. Kniveton, C. Kummerow, G. Liu, F. Marzano, A. Mugnai, W. Olson, G. Petty, A. Shibata, R. Spencer, F. Wentz, T. Wilhelm, and E. Zipser, 1998: Results of the WetNet PIP-2 project. *J. Atmos. Sci.*, **55**, 1483–1536.
- Smith, E. A., G. Asrar, Y. Furuhashi, A. Ginati, C. Kummerow, V. Levizzani, A. Mugnai, K. Nakamura, R. Adler, V. Casse, M. Cleave, M. Debois, J. Durning, J. Entin, P. Houser, T. Iguchi, R. Kakar, J. Kaye, M. Kojima, D. Lettenmaier, M. Luther, A. Mehta, P. Morel, T. Nakazawa, S. Neeck, K. Okamoto, R. Oki, G. Raju, M. Shepherd, E. Stocker, J. Testud, and E. Wood, 2007: International global precipitation measurement (GPM) program and mission: An overview. *Measuring precipitation from space EURAINSAT and the future*, Springer, 213–224.
- Sorooshian, S., K. Hsu, X. Gao, H. V. Gupta, B. Imam, and D. Braithwaite, 2000: Evaluation of PERSIANN system satellite-based estimates of tropical rainfall. *Bull. Amer. Meteor. Soc.*, **81**, 2035–2046.
- Spencer, R. W., H. M. Goodman, and R. E. Hood, 1989: Precipitation retrieval over land and ocean with SSM/I: Identification and characteristics of the scattering signal. *J. Atmos. Oceanic Technol.*, **6**, 254–273.
- Takeda, T., and K. Takase, 1980: Radar observation of rainfall system modified by orographic effects, *J. Meteor. Soc. Japan*, **58**, 500–516.
- Tian, Y., and C. D. Peters-Lidard, 2007: Systematic anomalies over inland water bodies in satellite-based precipitation estimates. *Geophys. Res. Lett.*, **34**, doi:10.1029/2007GL030787.
- Tian, Y., C. D. Peters-Lidard, B. J. Choudhury, and M. Garcia, 2007: Multitemporal analysis of TRMM-Based satellite precipitation products for land data assimilation applications, *J. Hydrometeorol.*, **8**, 1165–1183.
- Turk, F. J., and S. Miller, 2005: Toward improving estimates of remotely sensed precipitation with MODIS/AMSR-E blended data techniques, *IEEE Trans. Geosci. Remote Sens.*, **43**, 1059–1069.
- Turk, F. J., and A. V. Mehta, 2007: Toward improvements in short-time scale satellite-derived precipitation estimates using blended satellite technique. *Measuring precipitation from space EURAINSAT and the future*, Springer, 281–290.
- Ushio, T., K. Sasashige, T. Kubota, S. Shige, K. Okamoto, K. Aonashi, T. Inoue, N. Takahashi, T. Iguchi, M. Kachi, R. Oki, T. Morimoto, and Z.-I. Kawasaki, 2009: A Kalman filter approach to the Global Satellite Mapping of Precipitation (GSMaP) from combined passive microwave and infrared radiometric data, *J. Meteor. Soc. Japan*, **87A**, 137–151.
- Vila, D., R. Ferraro, and R. Joyce, 2007: Evaluation and improvement of AMSU precipitation retrievals, *J. Geophys. Res.*, **112**, D20119, doi:10.1029/2007JD008617.
- Wilheit, T. T., 1986: Some comments on passive microwave measurement of rain. *Bull. Amer. Meteor. Soc.*, **67**, 1226–1232.

- Wilheit, T. T., A. T. C. Chang, and L. S. Chiu, 1991: Retrieval of monthly rainfall indices from microwave radiometric measurements using probability distribution functions. *J. Atmos. Oceanic Technol.*, **8**, 118–136.
- Wilks, D. S., 2006: *Statistical Methods in the Atmospheric Sciences*, 2nd ed. Academic Press. 467 pp.
- Xie, P., and P. A. Arkin, 1996: Gauge-based monthly analysis of global land precipitation from 1971 to 1994. *J. Geophys. Res.*, **101**, 19023–19034.
- Xie, P., A. Yatagai, M. Chen, T. Hayasaka, Y. Fukushima, C. Liu, and S. Yang, 2007: A gauge-based analysis of daily precipitation over East Asia. *J. Hydrometeor.*, **8**, 607–626.
- Zhao, L., and F. Weng, 2002: Retrieval of ice cloud parameters using the AMSU. *J. Appl. Meteor.*, **41**, 295–384.